International Journal of Cosmetic Science

International Journal of Cosmetic Science, 2013, 1–6 doi: 10.1111/ics.12031

Measurement of stress–strain behaviour of human hair fibres using optical techniques

J. Lee and H. J. Kwon
Department of Mechanical and Mechatronics Engineering, University of Waterloo, 200 University Avenue West, Waterloo N2L 3G1, ON, Canada

Received 04 July 2012, Accepted 08 December 2012

Keywords: DIC, Hair, Poisson's ratio, True stress–strain

Synopsis

Many studies have presented stress–strain relationship of human hair, but most of them have been based on an engineering stress–strain curve, which is not a true representation of stress–strain behaviour. In this study, a more accurate 'true' stress–strain curve of human hair was determined by applying optical techniques to the images of the hair deformed under tension. This was achieved by applying digital image cross-correlation (DIC) to 10× magnified images of hair fibres taken under increasing tension to estimate the strain increments. True strain was calculated by summation of the strain increments according to the theoretical definition of 'true' strain. The variation in diameter with the increase in longitudinal elongation was also measured from the 40× magnified images to estimate the Poisson's ratio and true stress. By combining the true strain and the true stress, a true stress–strain curve could be determined, which demonstrated much higher stress values than the conventional engineering stress–strain curve at the same degree of deformation. Four regions were identified in the true stress–strain relationship and empirical constitutive equations were proposed for each region. Theoretical analysis on the necking condition using the constitutive equations provided the insight into the failure mechanism of human hair. This analysis indicated that local thinning caused by necking does not occur in the hair fibres, but, rather, relatively uniform deformation takes place until final failure (fracture) eventually occurs.

Résumé

De nombreuses études ont présenté des relations contrainte-déformation d'un cheveu humain, mais la plupart d'entre elles ont été fondées sur courbe contrainte-déformation artificielle qui n'est pas une vraie représentation du comportement contrainte-déformation. Dans cette étude, une mesure plus précise, une "vraie" courbe contrainte-déformation d'un cheveu humain a été déterminée en appliquant des techniques optiques aux images des cheveux déformés sous tension. Ceci fut obtenu en appliquant sur la corrélation croisée (DIC) des images numériques agrandies 10X des cheveux prises sous tension croissante pour estimer les incréments de déformation. La déformation vraie a été calculée par sommation des incréments de déformation en fonction de la définition théorique de la «vraie» tension. La variation de diamètre avec l'augmentation de l'allongement longitudinal est également mesurée à partir des images agrandies 40X, afin d'estimer le coefficient de Poisson et le stress vrai. En combinant la vraie tension et le stress vrai, une véritable courbe contrainte-déformation peut être déterminée, qui a montré les valeurs des contraintes beaucoup plus élevés que la courbe contrainte-déformation conventionnelle au même degré de déformation. Quatre régions ont été identifiées dans la vraie relation contrainte-déformation et des équations empiriques équations constitutives ont été proposées pour chaque région. L'analyse théorique de la condition de striction en utilisant les équations constitutives de la condition permet de mieux comprendre le mécanisme de rupture du cheveu humain.

Cette analyse a révélé qu'un amincissement local causé par striction ne se produit pas dans les fibres capillaires, mais, plutôt, une déformation relativement uniforme a lieu jusqu'à la finale défaillance (rupture).

Correspondence: Hyock Ju Kwon, Department of Mechanical and Mechatronics Engineering, University of Waterloo, 200 University Avenue West, Waterloo, N2L 3G1, ON, Canada. Tel: (519) 888-4567 (ext) 33427, Fax: (519) 885-5862; e-mail: hjkwon@uwaterloo.ca

Introduction

Human hair is the filamentous appendage of the skin serving to protect the body mainly against coldness and wetness [1]. It is a complex filamentous nanocomposite biomaterial, primarily composed of keratin, a fibrous protein rich in the amino acid cysteine [2]. As strong, healthy and beautiful hair has been universally desired across various cultures, it has been the topic of many studies from various disciplines. Human hair fibres are stressed under tensile forces as they are combed, groomed and styled; thus, many of the studies have focused on the mechanical properties in tension.

Theoretical models have been proposed to interpret experimental tensile stress–strain curves of wool, hair and other α-keratin fibres using structural mechanics [3]. Goldsmith and Baden [4] measured the stress–strain curve and the instantaneous Young's modulus of hair by employing sonic velocity measurement. A multiscale modelling approach to link mechanical properties of human hair fibres to structural information was discussed by Akkermans and Warren [3, 5]. Microscopic simulations of keratin proteins, mesoscale modelling of a macrofibril and a theoretical macroscopic model were used to link the microscopic scale to macroscopic observables, i.e. experimental stress–strain curves. Seshadri and Bhushan [6] estimated the stress–strain curve of human hair using an atomic force microscope and a custom built tensile sample stage.

However, all of the stress–strain curves presented mentioned above are engineering stress–strain curves, which do not represent the true instantaneous stress–strain responses. The primary reason

of scarcity of the information on true stress–strain behaviour is the lack of capability of in-situ measurement of cross-sectional area change during longitudinal deformation. Note that hair diameter is not constant, but varies significantly (more than 10%) along the length, even in the small segment of healthy hair. Therefore, both stress and strain are not uniform along the length, but alter considerably. If the strain is calculated from the displacement between grippers (i.e. the fibre fixing points) and the stress is estimated from the load and the cross-sectional area at a specific location, as in the conventional scheme [3, 6], then the determined engineering stress–strain curve is just the relationship between averaged stress and averaged strain in the gauge section, sometimes very different from the real stress–strain behaviour. Note that cross-sectional diameter and shape of hair fibres is highly associated with ethic groups. Franbourg *et al.* [7] reported that Asian hair has a greater diameter with circular geometry, while African hair presents a high degree of irregularity in the diameter of hair along the hair shaft with an elliptic section. Caucasian hair has an intermediate diameter and section shape. Therefore, particular attention should be paid to the calculation of stress. Stress concentration at the gripper can also frequently cause strain localization leading to premature fracture at the gripped region and therefore afford erroneous results.

Despite Poisson's ratio being a fundamental parameter characterizing the mechanical behaviour of a material [6, 8], only a handful of studies have examined the Poisson's ratio of human hair, because of the difficulty in evaluating transverse strain. An intensity correlation method has previously been employed to estimate diamter change owing to axial loading in a small strain range [9, 10]; however, a measure of the continuous variation in Poisson's ratio across a large strain range has not been reported so far.

In this study, the true stress–strain curve and the variation in the Poisson's ratio were determined by applying digital image correlation to two types of images obtained by CCD cameras with 10× and 40× objective lenses respectively. It was found that the measured true stress–strain curve lies at much higher values than the engineering stress–strain curve, with the true failure stress being higher than that of the engineering counterpart by more than double. As only one individual's hairs were used and the number of samples was small, the stress–strain behaviour presented here is not statistically significant. However, this study sets the basis for further studies on a range of individuals and hair types.

Materials and Methods

Measurement system

Tensile tests were performed using a TA micro testing machine (TA.xt Plus, Stable Micro Systems, Surrey, U.K.) with a 1-kgf load cell. During the tests, force, displacement and time were recorded by the computer while the images of hair sample were captured at 5 frames per second by two high resolution CCD cameras (1028 × 1008 pixels, STC-CL202A, SENTECH, Kanagawa, Japan.) with a 10× and 40× objective lens simultaneously, as shown in Fig. 1(a). Mechanical testing and image capturing were synchronized and controlled by an in-house developed LabVIEW (National Instrument, Austin, TX, U.S.A.) program. Pixel sizes in the images acquired by 10× and 40× objective lenses were 0.37 and 0.095 μm respectively.

To suppress stress concentration at the gripped sections, both ends of the sample were wound around the round bars before being gripped by custom-built grippers as shown in Fig. 1(b). Strain localization was effectively suppressed and failure almost always happened in the gauge section.

Sample preparation

Hair samples were collected from the back of the head (vertex posterior) of a healthy Asian woman in early twenties. No specific treatment was applied to the sample. Sample diameter measured by a micrometer (Mitutoyo Series 293, 1 μm resolution) was varied from 50 to 70 μm between different samples. In the same sample, diameter varied up to $\pm$5 μm along the length. Cross-sectional circularity was assessed by repeatedly measuring the diameter of the samples at different angles of rotation. The deviations from the mean diameter were less than 2%, thus the cross-sections of the samples were regarded as circular. This is consistent with the literature reporting that Asian hair has a circular cross-section [7]. The diameter measured by micrometer was only for reference and not used for calculating stress or strain. More than 20 samples were tested for statistical analysis.

No pre-treatment of the hair fibre surfaces was necessary prior to taking their images for DIC. Indeed, the natural features of surface roughness on the fibres provided a convenient pattern for tracking the surface movement in the DIC.

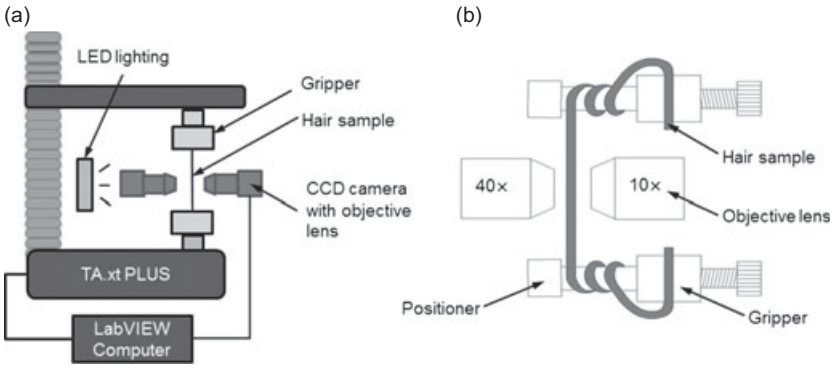

Figure 1 Schematics of testing setup: (a) tensile testing equipment; and (b) gripper details.

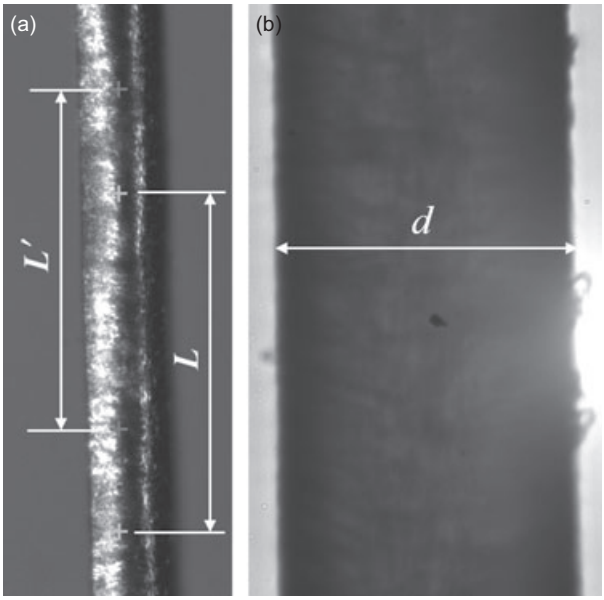

Figure 2 (a) 10× magnified image of hair with DIC grid points: L is the reference length and L' is the deformed reference length; (b) 40× magnified image of hair: d is the hair diameter.

True strain measurement

Theoretically, true strain can be obtained by integrating strain increment. Strain increment between images at different degrees of deformation was calculated according to Eq. (1):

$$\delta\varepsilon = \delta L/L \tag{1}$$

where L is the reference length and δL the elongation in L. L was taken to be 700 pixels (245 μm) and δL was measured by applying a custom-developed digital image cross-correlation (DIC) algorithm to 10× images ($\delta L = L' - L$ in Fig. 2(a)). Instead of integration, true strain could be calculated by summation of strain increments over the images according to Eq. (2):

$$\varepsilon = \sum \delta\varepsilon_i = \sum \delta L_i/L_i \tag{2}$$

where $\delta\varepsilon_i$, δL_i and L_i are strain increments, elongation increments and reference length over a number of images N respectively.

Note that average true strain (ε_T)can also be calculated from average engineering strain (ε_E) using the following relationship shown in Eq. (3):

$$\varepsilon_T = \ln(1+\varepsilon_E) = \ln\left(1+\frac{\Delta}{L_0}\right) \tag{3}$$

where Δ is the cross-head displacement and L_0 the distance between grippers (or gauge length).

True stress estimation

True stress was estimated by dividing the measured force P by instantaneous cross-sectional area A according to Eq. (4):

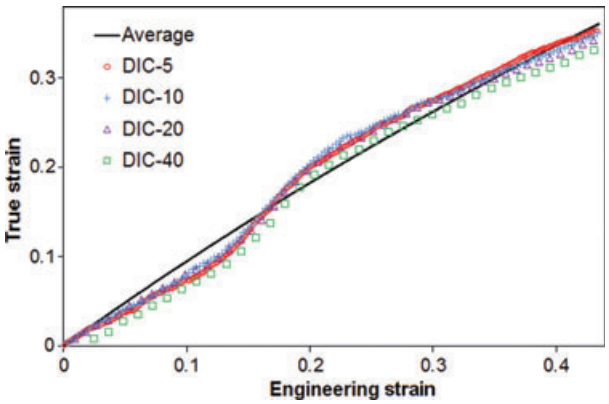

Figure 3 Plots of true strains against engineering strain. Engineering strain was calculated from the gripper displacement and converted into average true strain using Eq. (3). True strains were obtained by summating the strain increments, which were estimated every 5 images (DIC-5), 10 images (DIC-10), 20 images (DIC-20) and 40 images (DIC-40).

$$\sigma = \frac{P}{A} = \frac{4P}{\pi d^2} \tag{4}$$

where d was the instantaneous diameter measured from the 40× image by counting the pixels between both sides of the hair (Fig. 2(b)).

Results, Discussion and Conclusions

True strain

The elongation (δL) of the reference length L was measured by tracking the movements of the grid points at both ends, as shown in Fig. 2(a). To comply with the definition of true strain, the elongation increments (δL_i) and the strain increments ($\delta\varepsilon_i$) should ideally be infinitesimal, thus the number of increments needs to be as large as possible. Around 1500 images were acquired from each test, so that maximum number of increments could be obtained when the increments were estimated at each image. However, previous study [11] indicated that when the displacement between correlated images was less than one pixel, DIC accuracy was significantly reduced because of the inherent discontinuity of pixel-based DIC analysis.

The effect of the increment size on the strain accuracy was investigated by estimating the elongation increment (δL_i) and strain increment ($\delta\varepsilon_i$) at every 5, 10, 20 and 40 images, respectively, and calculating the true strains using Eq. (2). Grid points were also redefined at every 5, 10, 20 and 40 images, respectively, so that reference length was maintained at a constant throughout the calculations ($L_i = L$). Representative true strains estimated by Eq. (2) based on four different increment sizes, as well as average true strain calculated by Eq. (3), are plotted against the average engineering strain in Fig. 3.

True strains obtained by summation of the strain increments estimated at every 5, 10 and 20 images (DIC-5, DIC-10 and DIC-20 in Fig. 3) were almost overlapped with one another, except at the rightmost region where DIC-5 was the highest followed by DIC-10 and DIC-20. However, when the increments were estimated at every

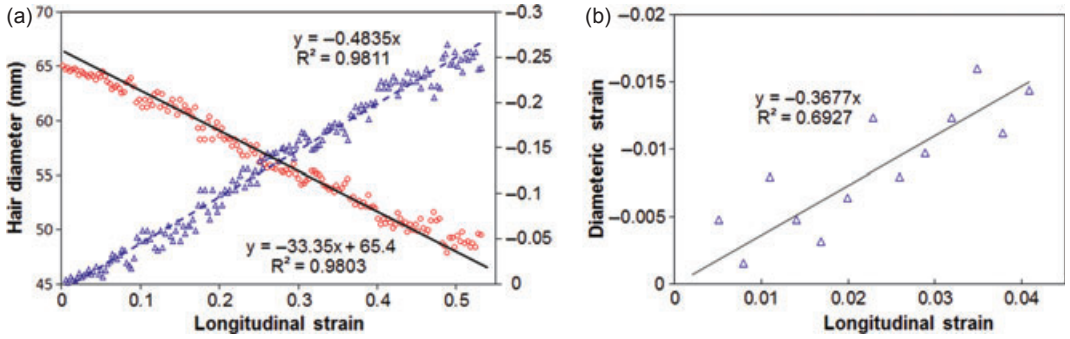

Figure 4 (a) The plots of hair diameter and the diametric strain with the increase in longitudinal strain, and (b) the plot of diametric strain in small strain region.

40 images (DIC-40), the calculated true strains were lower than the other three true strains across the entire range. Note that as the size of increments decreased, the calculation scheme in Eq. (2) became closer to the theoretical definition of true strain, thus more accurate results are obtained using this approach. However, the elongation increments estimated at every five images were sometimes as small as around one pixel (~0.37 μm), below which DIC accuracy is significantly reduced [11]. Also, DIC-5 and DIC-10 were almost coincident across entire strain range. Therefore, it was concluded that the true strains obtained by summation of the strain increments at every 10 images were most reasonably accurate in the proposed scheme and were adopted in the rest of the study.

Compared to the almost linear increase in the average true strain, all true strain curves estimated by DIC showed a trend towards non-linearly increasing trend, with lower than average values below 0.17 strain, and higher than average values at higher strain. A possible reason for this could be the non-uniform sample diameter along the length, as previously discussed in 'Sample preparation'.

Poisson deformation

When the sample was elongated in the axial direction, Poisson deformation occurred in the lateral direction, causing a change in diameter. The sample diameter at the middle of the reference length was measured using the 40× image (Fig. 2(b)), and plotted against the engineering strain in Fig. 4(a).

The sample diameter was around 65 μm in the undeformed state, but kept decreasing to less than 50 μm until failure occurred at around 0.52 engineering strain. The decreasing trend seems to be almost linear; however, close observation suggested that more data points reside under the trend line in the region below 0.15 engineering strain, while more data points exist above the trend line at higher strains.

Diametric engineering strain (ε_d) was calculated using the measured diameter d and the initial diameter d_0 according to Eq. (5)

$$\varepsilon_d = \frac{d - d_0}{d_0} \tag{5}$$

and plotted on Fig. 4(a) using the secondary coordinate in the right side. Note that the right vertical axis was reversed to minimize the overlapping with diameter plots. Similar trend was identified as the diameter, i.e. diametric strains were slightly under the trend line below 0.15 strain, but above the trend line at higher strains.

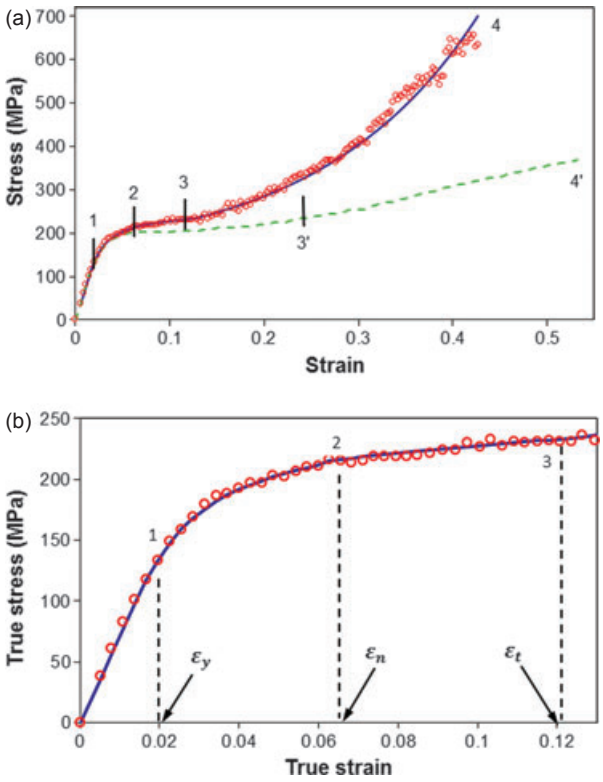

Figure 5 (a) The plots of hair diameter (○) and the diametric strain (△) with respect to the longitudinal strain, and (b) the plot of diametric strain in small strain region.

The Poisson's ratio could be determined from the slope of the diametric strain vs. longitudinal strain plots. Poisson's ratio has greater importance in the small strain region, as many biological materials exhibit volume change during elastic deformation [12]. Close observation on the small strain region (ε) suggested that the Poisson's ratio was around 0.38 in this region, as shown in Fig. 4(b). For multiple samples, the Poisson's ratio was determined

Table I Constants in Eq. (6) before yielding, $\varepsilon \leq \varepsilon_n$

Constant	E	ε_y	ε_n	a	b	c	d
Value	7000 MPa	0.015	0.063	−120	60	−0.065	111.7

Table II Constants in Eq. (6) after yielding, $\varepsilon \leq \varepsilon_n$

Constant	ε_t	K	N	k	M	β
Value	0.12	300	0.12	200	5	1.6

to be 0.37 ± 0.05, which indicated that slight volume increase occurred when the deformation was small. This value is close to the previously reported value (0.377) measured by laser diffraction method [10].

The Poisson's ratio across a large strain region could be estimated by the slope in Fig. 4(a). Note that the variation in Poisson's ratio of the hair across a large strain region has rarely been reported. Hu *et al.*'s measurement [10] was limited to a small strain region less than 0.04. The plots in Fig. 4(a) were almost linear across the entire region with the constant slope of around −0.48. For multiple samples, the overall Poisson's ratio was estimated to be 0.48 ± 0.03, suggesting that the deformation occurred in almost an incompressible manner and volume was conserved at large deformation.

True stress–strain curve

Using the diameter change during the tensile deformation, true stress could be calculated using Eq. (4), based on the assumption of circular cross-section [7]. By combining this with the true strain, the true stress–strain relationship could be determined, as presented in Fig. 5. Compared with the engineering stress–strain curve (dotted curve in Fig. 5), the true stress–strain relationship demonstrated much higher stress at the same strain, particularly in the large strain region. It also exhibited a fast rising curve with the increase in strain, indicating that significant strain-hardening was involved in the deformation of hair.

Goldsmith and Baden [4] divided the engineering stress–strain curve into three regions: 1) Hookean region with rapid increase in stress up to 2% strain (0–1 in Fig. 5(a)); 2) yield region with very little increase in stress up to 25% strain (1–3′); and 3) post-yield region (3′–4′) with sharply increasing stress with increasing strain. However, the divisions were somewhat arbitrary and no detailed rationale is given for them.

If the same stress–strain data are plotted on a true stress-true strain plane, four different regions can be identified with different trends: 1) linear elastic region (Hookean region) (0–1 in Fig. 5(a)); 2) non-linear transition region (1–2) where transition from linear elastic to plastic occurred; 3) yield region (2–3) where the curve is almost flat; and 4) hardening region (3–4) where the stress increases exponentially against the strain. Each region can be fitted to the following empirical constitutive equations:

$$\sigma = \begin{cases} E\varepsilon & (\varepsilon \leq \varepsilon_y) \quad (6a) \\ \left[(b\varepsilon)^{(c-1)} - (b\varepsilon)^{-c}\right] + d & (\varepsilon_y \leq \varepsilon \leq \varepsilon_n) \quad (6b) \\ \varepsilon^N & (\varepsilon_n \leq \varepsilon \leq \varepsilon_t) \quad (6c) \\ \exp\left(M\varepsilon^\beta\right) & (\varepsilon_t \leq \varepsilon) \quad (6d) \end{cases}$$

where the constants are presented in Tables I and II. The plots in the region 1), 2) and 3) are magnified in Fig. 5(b), which shows excellent agreement between the experimental data and the trend curves. For multiple samples, the elastic modulus E was estimated to be 7.0 ± 0.3 GPa.

Failure mechanism

Failures in ductile materials in tension are frequently caused by necking where strain is concentrated at a small region of the material. In the necking process, the strength increase by strain-hardening is less than the stress increase by the reduction in cross-section [13–15]. So, if a particular cross-section becomes infinitesimally smaller than the remainder of the material, all subsequent deformation will concentrate at that section until final failure. Failure by unstable necking can be identified by significant local thinning at the failed section.

Under uniaxial loading condition, the condition for necking [14] is given in Eq. (7)

$$\frac{1}{\sigma}\frac{d\sigma}{d\varepsilon} \leq 1 \quad (7)$$

By substituting the third and fourth equations in Eq. (6) into Eq. (7), the following necking conditions can be derived:

$$\varepsilon \geq N = 0.12 \quad (8a)$$

$$\varepsilon \leq \left(\frac{1}{M\beta}\right)^{1/(\beta-1)} = 0.03125 \quad (8b)$$

Note that Eq. (8a) is the necking condition in region 3 and Eq. (8b) in region 4. According to these conditions, necking is initiated at $\varepsilon = 0.12$. However, this is the upper bound of region 3 (ε_t in Fig. 5(b)), and immediately after the neck is formed, the true stress–strain behaviour falls into region 4 and the necking condition is changed to Eq. 8(b). As the necking range in Eq. 8(b) is much less than the lower bound of region 4, necking cannot continue in region 4 and the initiated neck in region 3 cannot thus propagate to reach failure.

This analysis provides insight into the failure mechanism of hair. When the hair is loaded in tension, irregularities on the surface cause the stress concentration and strain localization at a particular section. This section might be locally deformed up to the maximum range of region 3; however, the neck initiation would lead to much higher strain-hardening rate than the cross-sectional reduction rate in region 4, thus the neck ceased to form any further in that section, but propagates into the neighbouring section in a stable manner. As the maximum range of necking was relatively low ($\varepsilon = 0.12$), macroscopically the hair seemed to be uniformly deformed across the entire length. Therefore, it is believed that final failure was not attained by the local reduction in cross-sectional area, but by the scission of keratin chains in a brittle manner. This was consistent with the experimental results, which showed a relatively uniform decrease in diameter across the entire length until final failure, without any sign of local

thinning at the failed section. In accord with this, previous studies using scanning electron microscopy (SEM) [16, 17] also reported brittle mode failure, usually at the root end of the hair, beginning as a split through the cell layers of the cuticle followed by catastrophic transverse fracture across the entire cross-section.

Acknowledgements

The study was supported by Korea Institute for Advancement of Technology (KIAT) (under International Collaborative Research and Development Programme) and Natural Sciences and Engineering Research Council of Canada (NSERC) (under Discovery Grant).

References

1. Popescu, C. and Hocker, H. Hair – the most sophisticated biological composite material. *Chem. Soc. Rev.* **36**, 1282–1291 (2007).
2. Smith, J.R. and Swift, J.A. Lamellar subcomponents of the cuticular cell membrane complex of mammalian keratin fibres show friction and hardness contrast by AFM. *J. Microsc.* **206**, 182–193 (2002).
3. Hearle, J.W.S. A critical review of the structural mechanics of wool and hair fibres. *Int. J. Biol. Macromol.* **27**, 123–138 (2000).
4. Goldsmith, L.A. and Baden, H.P. The mechanical properties of hair I. the dynamic sonic modulus. *J. Investig. Dermatol.* **55**, 256–259 (1970).
5. Akkermans, R.L.C. and Warren, P.B. Multiscale modelling of human hair. *Philos. Trans. R. Soc. London Ser. A.* **362**, 1783–1793 (2004).
6. Seshadri, I.P. and Bhushan, B. In situ tensile deformation, characterization of human hair with atomic force microscopy. *Acta Mater.* **56**, 774–781 (2008).
7. Franbourg, A, Hallegot, P., Baltenneck, F., Toutain, C. and Leroy, F. Current research on ethnic hair. *J. Am. Acad. Dermatol.* **48**, S115–S119 (2003).
8. Mott, P.H., Dorgan, J.R. and Roland, C.M. The bulk modulus and poisson's ratio of "incompressible" materials. *J. Sound Vibrat.* **312**, 572–575 (2008).
9. Hu, Z., Li, G., Xie, H., Hua, T., Chen, P. and Huang, F. Measurement of Young's modulus and Poisson's ratio of human hair using optical techniques. *Proc. SPIE.* **7522**, 75222Q (2010).
10. Hu, Z., Xie, H., Hua, T. and Wang, Z. Advanced intensity correlation method for evaluating poisson's ratio of fiberlike material. *Rev. Sci. Instrum.* **80**, 013105 (2009).
11. Han, Y., Rogalsky, A.D., Zhao, B. and Kwon, H.J. The application of digital image techniques to determine the large stress-strain behaviors of soft materials. *Polym. Eng. Sci.* **52**, 826–834 (2012).
12. Jurvelin, J.S., Buschmann, M.D. and Hunziker, E.B. Optical and mechanical determination of poisson's ratio of adult bovine humeral articular cartilage. *J. Biomech.* **30**, 235–241 (1997).
13. Hill, R. General theory of uniqueness and stability in elastic-plastic solids. *J. Mech. Phys. Solids* **6**, 236–249 (1958).
14. Kwon, H.J. and Jar, P.-.B. The application of essential work of fracture concept to toughness characterization of high-density polyethylene. *Polym. Eng. Sci.* **47**, 1327–1337 (2007).
15. Kwon, H.J. and Jar, P.-.B. On the application of fem to deformation of high-density polyethylene. *Int. J. Solids Struct.* **45**, 3521–3543 (2008).
16. Brown, A.C. and Swift, J.A. Hair breakage: the scanning electron microscope as a diagnostic tool. *J. Soc. Cosmet. Chem.* **26**, 289–297 (1995).
17. Swift, J.A. The mechanics of fracture of human hair. *Int. J. Cosmet. Sci.* **21**, 227–239 (1999).